Equations of motion of a track cyclist: Active particle dynamics under strong geometric constraints

C. Clanet [*]
LadHyX, UMR 7646 du CNRS, Ecole Polytechnique, 91128 Palaiseau, France

P. Odier [†] and B. Pottier [‡]
ENS de Lyon, CNRS, Laboratoire de Physique, F-69342 Lyon, France

E. Brunet [§]
Fédération Française de Cyclisme, 1 rue Laurent Fignon, 78390 Montigny, France

(Received 7 February 2025; accepted 12 September 2025; published xxxxxxxxxx)

Using *in situ* measurements from the 2022 World Championships, we derive the equations of motion for a track cyclist as a coupled bicycle-rider-track system. A key observation is that instantaneous pedal power does not map directly onto bicycle speed because elastic compliance within the bicycle-rider assembly stores and releases energy over the crank cycle, introducing a phase lag between input power and translational motion. To resolve this, we develop a phase-averaging framework over the pedaling period that yields an effective, stiff dynamical system driven by cycle-averaged power. The resulting reduced model predicts the evolution of speed without requiring high-frequency pedal-level inputs. A central feature is the geometric coupling between rider dynamics and velodrome shape: the equations link wheel-frame velocity to the center-of-mass velocity through the local track curvature, accounting for banking and radius variations along the lap. Applied to competition data, the framework reproduces the measured speed evolution across straights and turns. Beyond track cycling, the phase-average method provides a general route to modeling propulsion in compliant, cyclic systems where input power is periodic but motion is governed by averaged dynamics.

DOI: 10.1103/vm6w-d487

I. INTRODUCTION

The mechanics of track cycling have been examined for more than a century, beginning with Bourlet's seminal analyses of bicycle motion and velodrome geometry [1–3], and later synthesized by Craig and Norton [4]. Modern formulations for rider dynamics build on energy-balance arguments and lumped drag models. Lukes *et al.* [5] highlighted the strong sensitivity of such models to environmental parameters and called for validation using detailed atmospheric and cyclist data. Fitton and Simons [6] incorporated crank-level power from an SRM meter into a refined mechanical model, but did not address the sampling-rate requirements nor the mapping between instantaneous pedal power and bicycle speed, leaving a key closure problem open.

An illustration of the race under consideration—the kilometre time trial by Melvin Landerneau at Saint-Quentin-en-Yvelines—is given in Fig. 1. We model the rider-bicycle system as an active particle of total mass M, characterized by the center-of-mass speed $V_G(t)$, and the muscular power input $P_m(t)$. Its dynamics obey the energy balance

$$\frac{d}{dt}(T+U) = P_m - P_f, \tag{1}$$

where $T = \frac{1}{2}MV_G^2$ is the kinetic energy, $U = Mgz$ the gravitational potential energy, and P_f the power lost to aerodynamic drag and rolling resistance. This generic formulation, in the spirit of de Groot *et al.* [7] and encompassing the equation in Ref. [5], is compact but encounters two difficulties that limit its predictive power for $V_G(t)$.

First, quantifying P_f with sufficient fidelity remains challenging despite longstanding recognition of the dominant drag



FIG. 1. Melvin Landerneau in the kilometer time trial at the 2022 World Championships at the Saint-Quentin-en-Yvelines National Velodrome. Copyright FFC—Photograph Patrick Pichon.

[*]Contact author: christophe.clanet@polytechnique.edu
[†]Contact author: philippe.odier@ens-lyon.fr
[‡]Contact author: basile.pottier@ens-lyon.fr
[§]Contact author: e.brunet@ffc.fr

 ©2025 American Physical Society

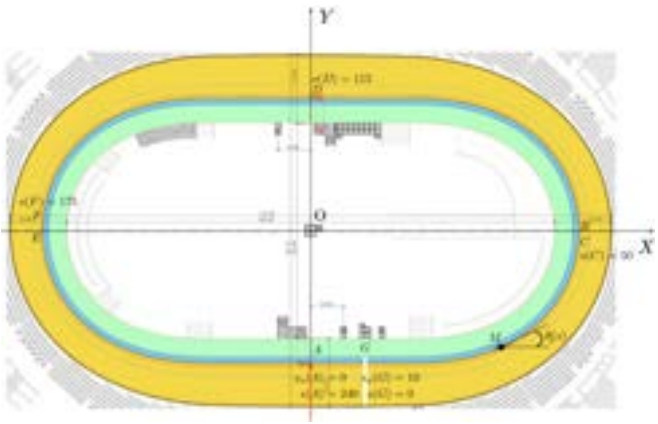


FIG. 2. Definition of the absolute reference frame (X, Y, Z) and the local coordinates s_a and s.

and rolling contributions [5,8,9]. Second, and more critically, the input $P_m(t)$ is neither monotonic nor smooth in time: field studies show a nonlinear dependence on speed [10], while high-frequency measurements reveal large intracycle oscillations [11].

The objective of this study is to determine how Eq. (1) must be modified and refined to establish a direct relationship between the instantaneous measured power $P_m(t)$ and the actual velocity of the bicycle $V(t)$, which can be different from $V_G(t)$ in a velodrome.

The paper is organized as follows. Section II documents the geometry of the Saint-Quentin-en-Yvelines track. The experimental dataset from Melvin Landerneau's kilometer time trial is described in Sec. III. Using these data, we first test the validity of Eq. (1) in Sec. IV, then introduce the phase-averaged model in Sec. V. The impact of turns and track curvature is analyzed in Sec. VI. Assumptions and limitations are discussed in Sec. VII, followed by conclusions.

II. VÉLODROME NATIONAL OF SAINT-QUENTIN-EN-YVELINES (SQY)

A. General characteristics of the Vélodrome National

The Vélodrome National of Saint-Quentin-en-Yvelines (SQY) opened on January 13, 2014. It was designed by the German architect Ralph Schürmann. A top-down architectural view is shown in Fig. 2, where the track is highlighted in yellow, the *Côte d'Azur* as the inner blue band, and the safety zone in green.

The official length of a velodrome is the length of the black line, located 20 cm from the *Côte d'Azur* (Fig. 3) and representing the calibrated racing path. To host the Olympic Games and UCI World Championships, this length must be exactly 250 m [12]. Three additional reference lines appear in Fig. 2: the red (sprinter's) line, 60-cm above the black line; the blue (stayer's) line, at one third of the track width; and the balustrade marking the outer boundary.

While the track width D_v is constant along the lap, its absolute value varies across venues. At SQY the width is $D_v = 8\,\mathrm{m}$, making it among the widest velodromes worldwide.

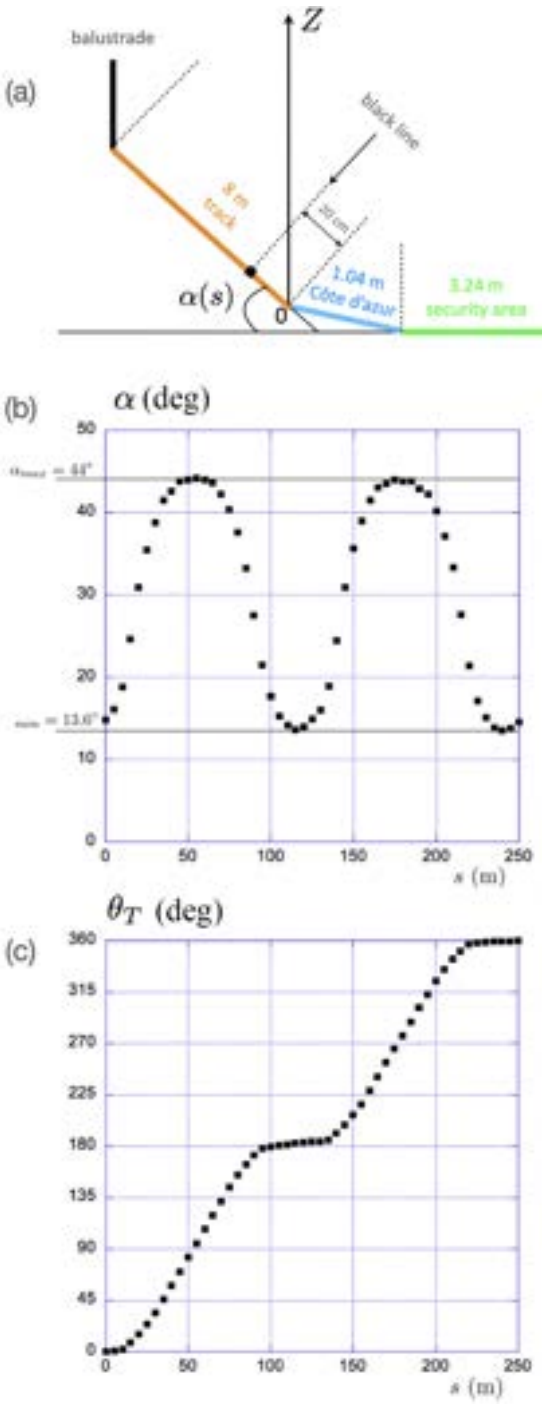


FIG. 3. (a) Schematic radial cut of the track; (b) measured banking angle $\alpha(s)$ along the black line; (c) measured azimuth $\theta_T(s)$.

B. Absolute reference frame X, Y, Z

We first locate points using a Cartesian frame with origin O at the geometric center of the velodrome. The horizontal axis OX aligns with the major axis, OY with the minor axis, and OZ is vertical upward (Fig. 2). In this frame, the coordinates (in meters) of key points on the black line are $A = (0, -24.29, 0)$, $B = (49.24, 0, 0)$, $D = (0, 24.29, 0)$, and $E = (-49.24, 0, 0)$.

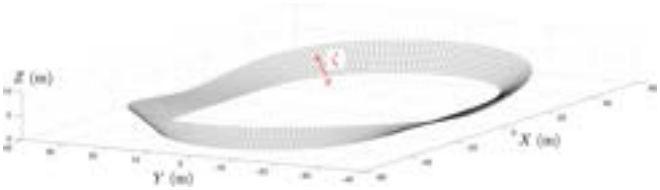


FIG. 4. Parametrization of points on the velodrome surface.

For analysis, this frame is inconvenient because O is not marked on the track. We therefore adopt a local curvilinear coordinate s_a along the black line, which is the fundamental metric of any velodrome and has total length $L_0 = 250\,\text{m}$ at SQY.

C. Absolute local coordinate s_a

Setting the origin at A so that $s_a(A) = 0$ induces $s_a(B) = 250/4 = 62.5$ m. Sporting convention, however, sets the zero at the finish line G, which fixes the ground markings. At SQY this corresponds to $s_a(G) = 10\,\text{m}$. This convention is venue dependent; for example, at the Izu Velodrome in Tokyo (also by Schürmann) the finish line is at $s_a(G) = 20\,\text{m}$.

D. Three useful local coordinates s, α, and θ_T

1. Local position s

The sports coordinate s is marked every 10-m along the black line, from $s(G) = 0$ to $s(G) = 250$ (both values are typically indicated at G). To fully describe the track surface, s is complemented by two angles: the banking angle α and the azimuth θ_T, both measurable with a clinometer.

2. Slope $\alpha(s)$

The banking angle α is defined in Fig. 3(a). Its measured variation along the black line is shown in Fig. 3(b). At SQY, α ranges from $\alpha_{\min} = 13.6^\circ$ on the straights to $\alpha_{\max} = 44^\circ$ in the turns, with representative values $\alpha(s = 240) = 13.6^\circ$ and $\alpha(s = 52.5) = 44^\circ$.

3. Azimuth $\theta_T(s)$

The azimuth $\theta_T(s)$ is the angle between the direction $\underline{OX}$ and the local tangent to the black line (Fig. 2). Over a complete lap, θ_T increases continuously from 0° to 360°. The measured variation at SQY is shown in Fig. 3(c).

4. Location of a track cyclist

As latitude and longitude specify a point on a sphere, two coordinates specify a point on the velodrome surface. From any point on the track, draw the normal to the black line (Fig. 4). Let ζ be the signed transverse distance from the black line, and let s be the corresponding projected curvilinear position along the black line. The pair (s, ζ) provides a complete parametrization of the surface.

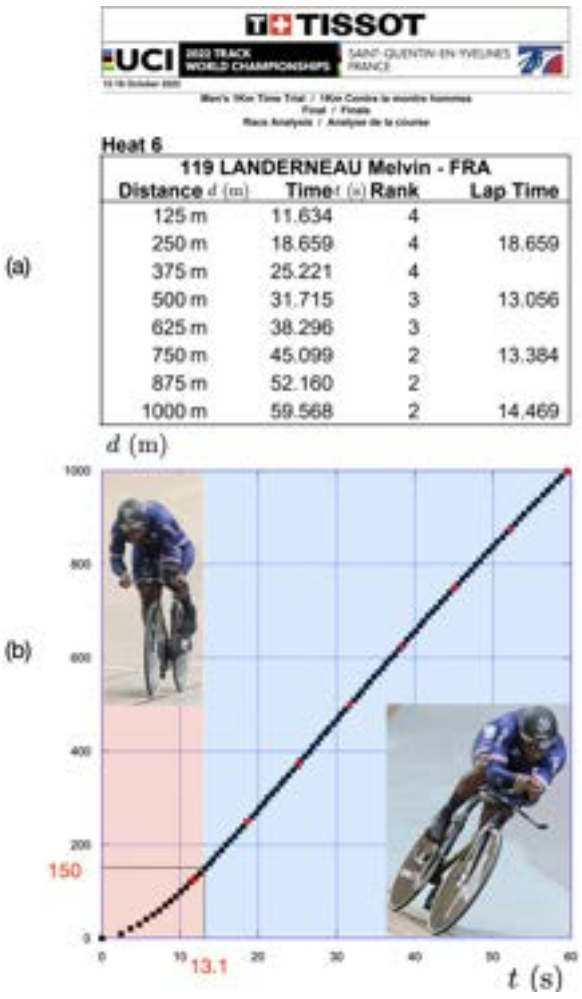


FIG. 5. (a) Official Tissot timing sheet; (b) time evolution of the distance traveled along the black line. Red symbols: Tissot intermediate splits; black symbols: video analysis.

III. EXPERIMENTAL DATA

A. 1-km time trial

The "kilo" is a standing-start time trial in which riders complete four laps in the shortest possible time. The shortest geometric path per lap lies at the junction between the *Côte d'Azur* and the track, but the sharp change in banking at this interface renders that trajectory unsafe in competition. Riders therefore target the black line, located 20 cm above the *Côte d'Azur* (i.e., $\zeta = 0$), throughout the race, as illustrated in Fig. 1.

In 2023, Jeffrey Hoogland set the "kilo" world record at 55.433 s at the Aguascalientes Velodrome (Mexico), surpassing the 56.303-s mark set by François Pervis in 2013. Historically the longest event contested by track sprinters, the kilo featured at the Summer Olympics from 1928 until its removal in 2008; it remains a marquee event at the UCI World Championships.

B. Official timing and video data

Figure 5(a) shows the timing sheet (time at every half lap) issued by the official timekeeper (Tissot) for Melvin

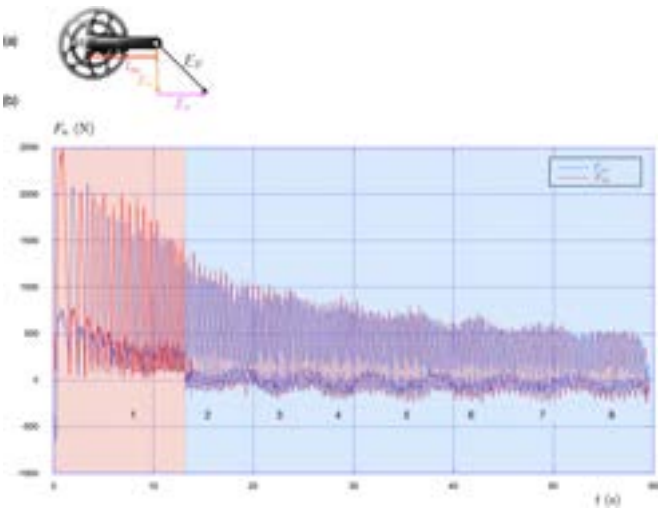


FIG. 6. (a) ZED crankset (Look) and decomposition of the total pedal force $\underline{F}_T$ into normal (F_n) and tangential (F_t) components. (b) Time series of F_n for each leg: left (F_{nl}, red) and right (F_{nr}, blue). Shading as in Fig. 5(b). The integers [1–8] refer to the turns.

Landerneau's final at the 2022 World Championships in which he finished second to Jeffrey Hoogland. The recorded finish time was 59.568 s; the lap-averaged speeds over the four laps were 48.2, 68.9, 67.2, and 62.2 km h^{-1}.

The National Velodrome (Saint-Quentin-en-Yvelines) is equipped with an automated multicamera video tracking system developed by the company Dartfish providing the distance traveled versus time, $d(t)$, shown in Fig. 5(b) (black symbols), together with the eight Tissot split points (red). After the standing start, the rider accelerates for 13.1 s before reaching an approximately steady speed of 66.4 km/h. Two posture phases are evident: an initial standing phase (red shading) associated with acceleration, followed by a seated, aerodynamic phase (blue shading) at nearly constant speed.

C. Instantaneous forces

1. Whole-race dynamics

The total cyclist-applied force $\underline{F}_T$ is decomposed into a propulsive component normal to the crank F_n and a nonpropulsive tangential component F_t; see Fig. 6(a). The normal force is sampled at 200 Hz using strain gauges integrated in each crank arm (sensor developed with Phyling [13]). Figure 6(b) reports F_n for the right (F_{nr}, blue) and left (F_{nl}, red) legs; positive values are propulsive, negative values resistive.

Peak forces exceed 2500 N at the start (left leg) and remain above 1500 N throughout the standing phase; the minima stay near zero. In the seated phase, peak forces decay progressively to ≈500 N, and shallow negative minima appear on both legs, indicating brief resistive contributions within the crank cycle. Across the entire race, intracycle force oscillations are clearly modulated at lap scale, with eight prominent envelopes corresponding to the eight turns of the 1-km event.

2. Standing phase (first 150 m)

During the first 13.1 s (≈150 m), Fig. 7(a) shows the right and left normal forces together with the pedaling rate $\dot{\theta}$ obtained from a crank-mounted gyroscope. The pedaling rate is zero over the initial 0.15 s (reaction time) and thereafter exhibits pronounced oscillations, with maxima aligned with force minima.

Given the instantaneous forces and pedaling rate, we compute the bicycle speed and muscular power as

$$V(t) = R\,G\,\dot{\theta}(t), \quad P_m(t) = [F_{nr}(t) + F_{nl}(t)]\;\ell_m\,\dot{\theta}(t),$$

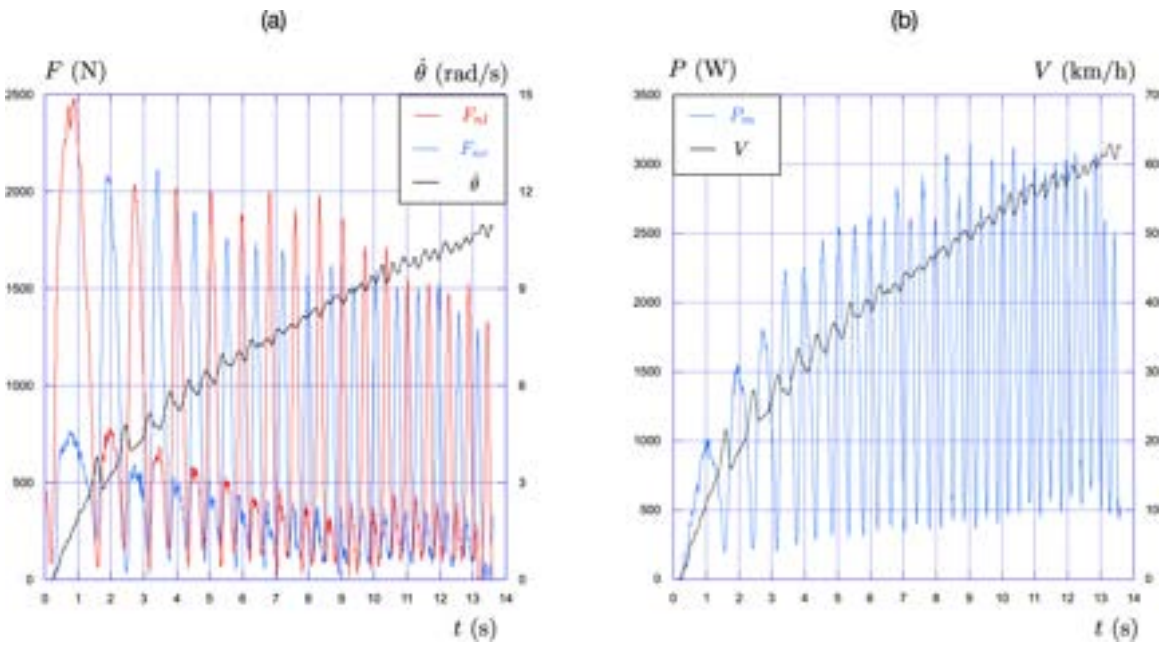


FIG. 7. Standing phase ($t \leqslant 13.1$ s). (a) Normal forces F_{nr} (blue) and F_{nl} (red) together with pedaling rate $\dot{\theta}$ (black) measured by gyroscope. (b) Instantaneous power $P_m(t)$ (blue) and bicycle speed $V(t)$ (black).

with wheel radius $R = 0.334$ m, crank length $\ell_m = 0.170$ m, and gear ratio $G = 62/13$ (single-speed, fixed-gear; ratio chosen prior to the race). Figure 7(b) shows that peak power grows from cycle to cycle, reaching up to 3100 W before saturating, while the speed increases monotonically to ≈60 km/h at the end of the standing phase. A salient feature is the phase opposition between $V(t)$ and $P_m(t)$: velocity maxima coincide with power minima.

IV. IS THE PHYSICAL MODEL CORRECT ?

Assuming the rider follows the black line throughout the kilometer time trial ($\zeta = 0$) so that z is constant, the energy balance in Eq. (1) reduces to a kinetic-dissipation balance for the center-of-mass (COM) speed $V_G(t)$:

$$\frac{dV_G^2}{dt} = \frac{2}{M}[\eta\, P_m(t) - P_f], \tag{2}$$

where $\eta \leqslant 1$ is a global efficiency converting crank power into forward mechanical power along the black line. This global efficiency η accounts for chain transmission, steering alignment, and internal rider-frame motions [9]. For the whole article we take $\eta = 0.92$. In Eq. (2) the dissipated power is modeled as

$$P_f = \tfrac{1}{2}\,\rho\,(SC_D + F)\,V_G^3 + C_{RR}Mg\,V_G.$$

The first term accounts for aerodynamic losses, drag (SC_D) [14] and the churning torque ($F = 0.006 \pm 0.001\,\mathrm{m}^2$ for lenticular wheels) [9,15], whereas the second term accounts for rolling resistance (C_{RR}).

For the standing posture, a wind-tunnel measurement gave a drag area $SC_D = 0.26 \pm 0.002$ m^2, and the air density during the 2022 World Championships at SQY was $\rho = 1.14 \pm 0.003$ kg m^{-3}. The rolling-resistance coefficient, measured on a drum bench [16] for a Vittoria Pista tire inflated to 12 bar was $C_{RR} = 0.0025 \pm 0.0002$. Using the total mass of rider $M_c = 92$ kg plus bicycle $M_b = 7.6$ kg, $M = M_c + M_b = 99.6$ kg, we numerically integrated Eq. (2) with the initial condition $V_G(0) = 0$, driven by the experimentally measured input power $P_m(t)$. The resulting theoretical COM speed $V_G(t)$ (red) is compared with the measured bicycle speed $V(t)$ (black) in Fig. 8.

The model reproduces the overall acceleration and saturation trends but fails to capture the large intracycle oscillations present in the measured velocity. This discrepancy indicates that Eq. (2), as used here, is incomplete. In particular, V_G is the COM speed of the rider-bicycle system, whereas the measurement V reflects the wheel-frame (bicycle) speed. During the standing phase the rider undergoes substantial body motion relative to the frame, so the instantaneous COM speed differs from the bicycle speed. A correct prediction of the observed velocity therefore requires augmenting the model to account for rider–frame compliance and the kinematic relation between COM and bicycle velocities.

V. PHASE-AVERAGED MODEL

Because the rider's configuration is periodic over a crank revolution, snapshots taken once per cycle with the crank at a fixed angle would show the rider in the same posture each

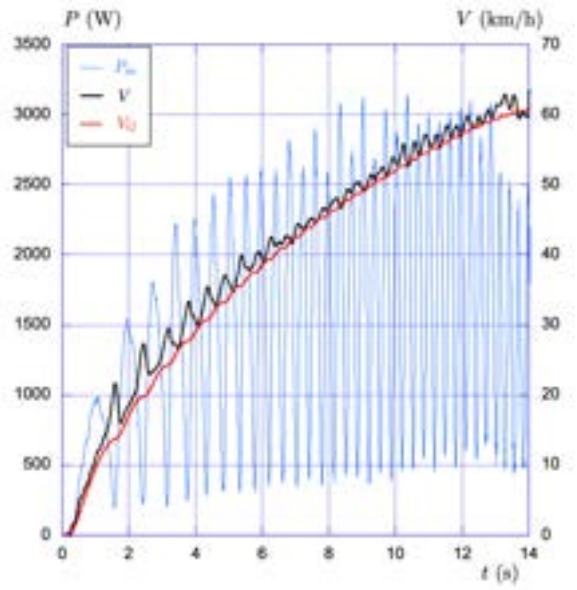


FIG. 8. Time evolution of the instantaneous power $P_m(t)$ (blue), measured bicycle speed $V(t)$ (black), and theoretical COM speed $V_G(t)$ (red) obtained from Eq. (2).

time. At this stroboscopic timescale the coupled rider-bicycle system behaves as an effective rigid body. This motivates applying a cycle-wise (phase) average to Eq. (2) so that fast intra-cycle motions are filtered out and only the slow evolution of speed is retained. We define the phase-averaging operator over the instantaneous period $T(t)$ as

$$\overline{q}(t) = \frac{1}{T(t)}\int_t^{t+T(t)} q(t')\,dt'. \tag{3}$$

This operation separates the fast crank-scale dynamics from the slower center-of-mass evolution on times much longer than a pedaling cycle. The instantaneous period $T(t)$ is defined using the cadence $\dot\theta(t)$ through the relationship

$$\int_t^{t+T(t)} \dot\theta(t')dt' = 2\pi\,. \tag{4}$$

The time evolution of the period $T(t)$ is plotted in Fig. 9(a) while the time evolution of the power $\bar P_m(t)$ and of the velocity $\bar V(t)$ are shown in Fig. 9(b). The mean power $\bar P_m(0) = 714$ W over the first pedal cycle $T(0) = 2.7$ s induces the initial velocity $\bar V_G(0) = 14.0$ km/h.

Averaging Eq. (2) yields the phase average evolution of the center-of-mass speed

$$\frac{d\overline{V}_G^2}{dt} = \frac{2}{M}\left[\eta\overline{P}_m(t) - \frac{1}{2}\rho(SC_D + F)\overline{V}_G^3 - C_{RR}Mg\overline{V}_G\right]. \tag{5}$$

Initially, the relationship $d\bar V_G^2/dt \approx 2\eta\bar P_m(0)/M$ leads to $\bar V_G(0) = \sqrt{\frac{8}{9}\frac{\eta\bar P_m(0)T(0)}{M}} = 3.97$ m/s (14.3 km/h) which is close to the value reported in Fig. 9(b). Using this value, $\bar V_G(0)$, for the initial condition of the average velocity, the numerical integration of Eq. (5) driven by the measured power $\overline{P}_m(t)$ produces the theoretical cycle-mean speed $\bar V_G$ (red) shown in Fig. 10. To extend the calculation to the full time trial, we account for the posture-dependent drag area, using $SC_D =$

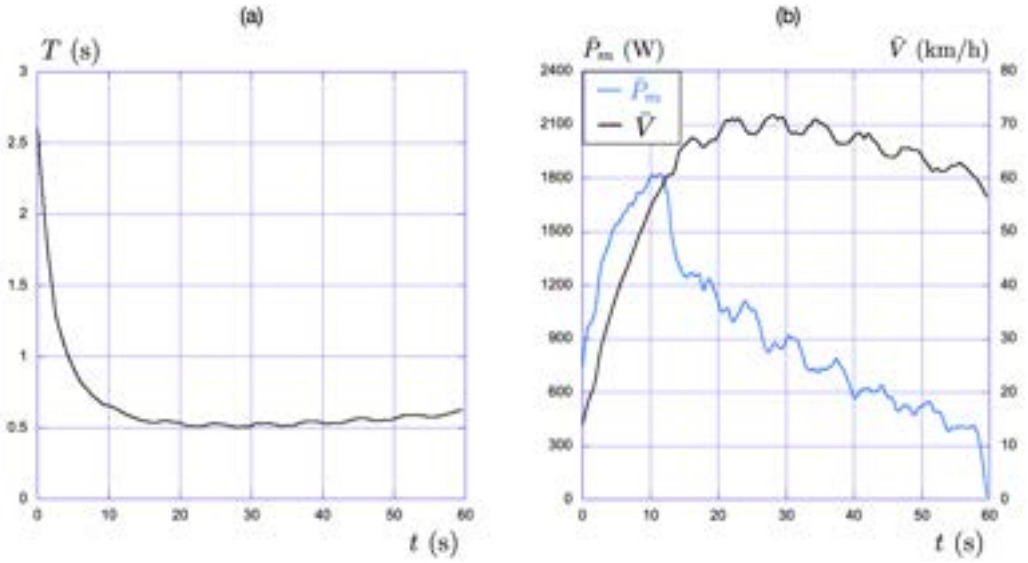


FIG. 9. (a) Time evolution of the instant period $T(t)$ defined by Eq. (4), (b) Time evolution of the average power $\bar{P}_m(t)$ and of the average velocity $\bar{V}(t)$ as defined by Eq. (3).

0.204 ± 0.002 m^2 in the seated phase. While the agreement during the standing phase is satisfactory (the first 13 seconds), systematic discrepancies appear in the turns, with the model underestimating the measured speed, indicating that geometric coupling to track curvature must be incorporated.

VI. IMPACT OF TURNS

Even after phase-averaging, the mean bicycle speed differs from the COM speed in turns. Figures 11(a) and 11(b) sketches a rider negotiating a bend; the COM lies a horizontal distance δ inward from the wheel contact line. The top view in Fig. 11(c) shows that the corresponding mean speeds satisfy

$$\overline{V} = \frac{\overline{V}_G}{1-\delta/R_c}, \quad \frac{\delta}{R_c} = \frac{L_G}{R_c}\,\frac{\frac{\overline{V}_G^2}{gR_c}}{\sqrt{1+\left(\frac{\overline{V}_G^2}{gR_c}\right)^2}}, \tag{6}$$

where R_c is the local radius of curvature of the black line, g is gravitational acceleration, and L_G is the vertical position of the COM above the wheel-ground contact line at mid-stance. The second relation follows from $\delta = L_G \cos\beta$ together with the lateral force balance in the plane normal to the trajectory, which gives $1/\tan\beta = \overline{V}_G^2/(gR_c)$ for the lean angle β [see Figs. 11(a) and 11(b)].

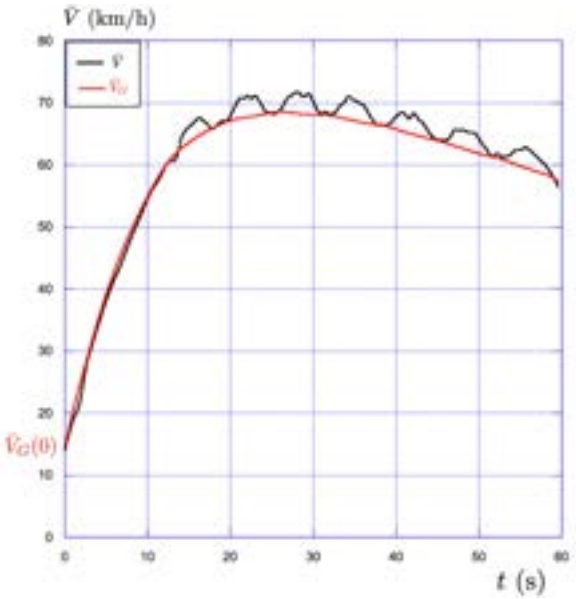


FIG. 10. Comparison between the experimental cycle-mean speed (black) and the theoretical result from Eq. (5) over the full kilometer.

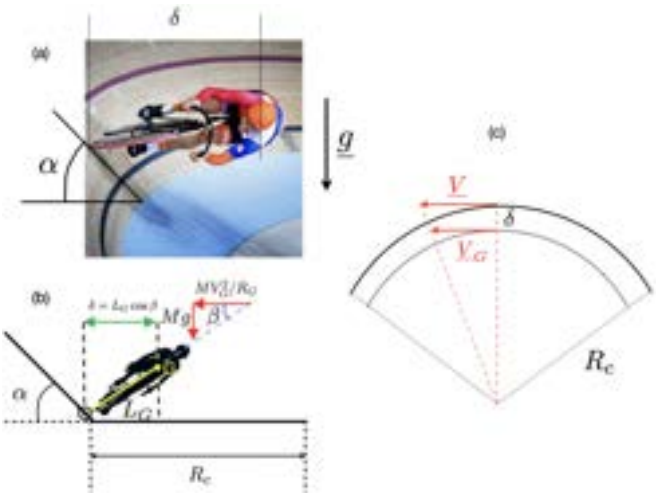


FIG. 11. (a) Lean of the track cyclist in a turn, (b) transverse equilibrium of the track cyclist in a turn, (c) geometric relation between the bicycle velocity $\underline{V}$ and the center-of-mass velocity $\underline{V}_G$.

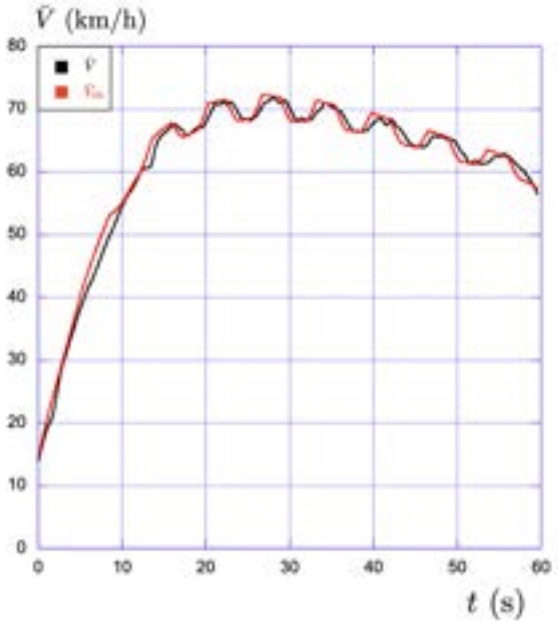


FIG. 12. Comparison between measured cycle-mean bicycle speed ($\overline{V}$, black) and the theoretical prediction ($\overline{V}_{\rm th}$, red) obtained by integrating Eqs. (5) and (6).

Along the black line, R_c is set by the measured azimuth $\theta_T(s)$ of the track via

$$\frac{\mathrm{d}\theta_T}{\mathrm{d}s} = \frac{1}{R_c(s)},$$

with $\theta_T(s)$ provided in Fig. 3. For a rider with height L_c, L_G is approximately constant: $L_G \simeq 0.75\,L_c$. For Melvin Landerneau this yields $L_G = 1.38\,\mathrm{m}$.

Two limiting cases are instructive. When $\overline{V}_G^2/(gR_c) \ll 1$ (straights; $R_c \to \infty$), Eq. (6) gives $\delta/R_c \ll 1$ and hence $\overline{V} = \overline{V}_G$. In the opposite limit $\overline{V}_G^2/(gR_c) \gg 1$ (tight, fast turns), $\delta \to L_G$ and

$$\overline{V} = \frac{\overline{V}_G}{1 - L_G/R_c}.$$

For SQY, $R_c \simeq 22\,\mathrm{m}$ at the center of turns. With $L_G = 1.38\,\mathrm{m}$ we get $\overline{V} \simeq 1.063\,\overline{V}_G$: the bicycle speed exceeds the COM speed by ≈6.6%. For $\overline{V}_G = 68\,\mathrm{km\,h^{-1}}$, Eq. (6) predicts $\overline{V} \simeq 72.5\,\mathrm{km\,h^{-1}}$, consistent with Fig. 10.

In practice, we first compute the COM speed, $\bar{V}_G$, from the phase-averaged dynamics Eq. (5) using the measured cycle-mean power $\overline{P}_m(t)$ and then map it to the bicycle speed with Eq. (6). Using the full-race $\overline{P}_m(t)$ [Fig. 9(b)], numerical integration of Eqs. (5) and (6) yields the theoretical bicycle speed $\overline{V}_{\rm th}$, which we compare to the measured cycle-mean speed $\overline{V}$ in Fig. 12. The close agreement demonstrates that the two-stage model (phase-averaged energetics for $\overline{V}_G$ combined with geometric correction for turns) accurately predicts bicycle speed on a given track once the cycle-averaged power is known.

VII. MINOR IMPROVEMENTS

Although the phase-averaged description captures the mapping between cycle-mean pedaling power and bicycle speed, several simplifying assumptions merit examination.

A. Single effective mass?

Throughout, the total mass has been taken as the sum of the rider and bicycle masses, $M = M_c + M_b$, with $M_c = 92\,\mathrm{kg}$ and $M_b = 7.6\,\mathrm{kg}$. This neglects the wheels' rotational inertia, which adds to the kinetic energy of the rider-bicycle COM:

$$T = \tfrac{1}{2}MV_G^2 + \tfrac{1}{2}J\omega^2 = \tfrac{1}{2}(M + M_i)V_G^2,$$

where $M_i \equiv J/R^2$ is the inertia-equivalent mass and R is the wheel radius. Measurements of bicycle-wheel moments of inertia using torsional-pendulum methods [17] indicate that, for track wheels, the nondimensional ratio $J/(M_wR^2)$ is typically 0.5, consistent with the wheels employed here. For a representative total wheel mass $M_w = 1.8\,\mathrm{kg}$, this yields $M_i \simeq 0.9\,\mathrm{kg}$. Relative to $M = 99.3\,\mathrm{kg}$, the resulting change in the kinetic energy T is of order 1%, well below the other uncertainties considered herein. For completeness, this correction can be absorbed into an effective mass $M_{\rm eff} = M + M_i$ without modifying the structure of the model.

B. On evaluating rolling ("solid") friction

The rolling-loss power is $C_{RR}\,F_N\,\overline{V}$, where F_N is the normal load on the tire and $\overline{V}$ the cycle-mean bicycle speed. Owing to track banking and rider lean (Fig. 11), F_N differs from the weight Mg and, under lateral force balance, reads

$$F_N = Mg\left(\cos\alpha + \frac{\overline{V}_G^2}{gR_c}\sin\alpha\right), \tag{7}$$

with local banking angle $\alpha = \alpha(s)$, COM speed $\overline{V}_G$, and curvature radius $R_c = R_c(s)$ along the black line, related to the measured azimuth $\theta_T(s)$ by $\mathrm{d}\theta_T/\mathrm{d}s = 1/R_c$ (see Figs. 2 and 3). Limiting cases are consistent: on a flat road ($\alpha = 0$), $F_N = Mg$; at high speed on a vertical wall ($\alpha = \pi/2$), $F_N = M\overline{V}_G^2/R_c$. Quantitatively, on SQY straights ($1/R_c = 0$, $\alpha = 13.6^\circ$), Eq. (7) gives $F_N \simeq 0.97\,Mg$. In turns ($R_c \simeq 22\,\mathrm{m}$, $\alpha = 44^\circ$) at $\overline{V} \approx 67\,\mathrm{km\,h^{-1}}$, it yields $F_N \simeq 1.84\,Mg$.

Approximating F_N by Mg thus underestimates rolling losses, especially in turns. However, because aerodynamic dissipation dominates, the impact on predicted speeds is modest. This is confirmed in Fig. 13, where using Eq. (7) to evaluate $C_{RR}F_N\overline{V}$ and integrating Eqs. (5) and (6) leads to predictions ($V_{\rm th}$, red) that remain in close agreement with measured cycle-mean speeds (V, black).

VIII. CONCLUSION

In this study, we investigated the equations of motion governing a track cyclist using field data recorded during the 2022 World Championship. Our analysis highlighted the complexity of relating instantaneous pedaling power to the velocity of the bike due to the deformability of the cyclist-bike system. The problem was solved introducing a phase-averaging

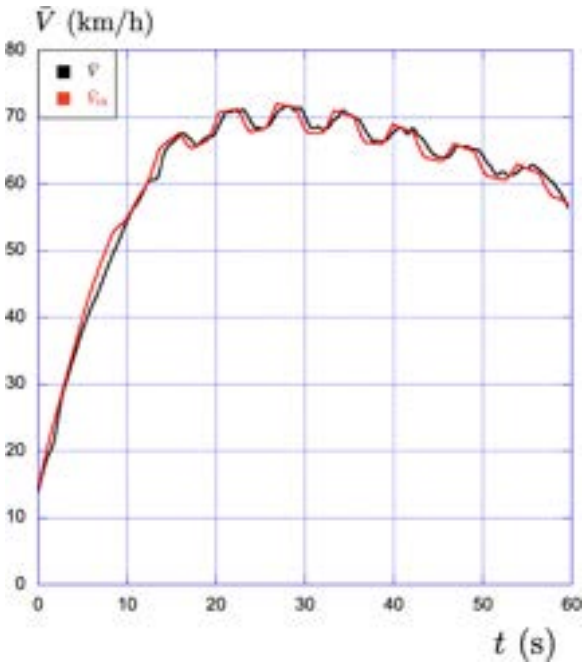


FIG. 13. Cycle-mean speed: experiment (V, black) versus theory ($V_{\rm th}$, red) obtained by integrating Eqs. (5) and (6), using Eq. (7) for the rolling-load F_N.

method that effectively rigidifies the system, allowing for a more accurate prediction of velocity evolution.

Furthermore, our results demonstrated that a single energy balance equation is insufficient to fully describe the system's dynamics. By incorporating a second equation that accounted for the geometrical constraints imposed by the velodrome, we developed a robust framework for predicting the bike velocity from the average pedaling power per cycle. This approach provides a fundamental tool for understanding performance optimization in track cycling and can be extended to other cyclic propulsion systems.

ACKNOWLEDGMENTS

We deeply thank Grégory Baugé for his generous and insightful discussions on sprint track cycling which greatly enriched this work through his personal experience. More generally, we thank the riders and staff of the French national track cycling teams for their steady collaboration and for welcoming physicists into their performance environment. Their openness and professionalism made this study possible. This work received funding from France 2030 under the Programme Prioritaire de Recherche "Sport de Très Haute Performance", operated by the Agence Nationale de la Recherche (ANR), Grant THPCA2024: ANR-265 2020-STHP2-0006. The funder had no role in study design, data collection and analysis, decision to publish, or preparation of the manuscript.

Melvin Landerneau provided written informed consent prior to participation. Data were collected during the 2022 World Championships, with no experimental manipulation or intervention introduced by this study. All procedures complied with the Declaration of Helsinki.

C.C. conceived analyses, developed the model, and drafted the manuscript; P.O. contributed to interpretation and finalized the writing; B.P. checked the model and contributed to interpretation; E.B. initiated the project and provided resources and supervision.

Language editing and formatting were assisted by AI-based tools; all scientific content, analyses, and interpretations were done by the authors.

DATA AVAILABILITY

The data and analysis code that support the findings of this study are available from the corresponding author upon reasonable request.

[1] C. Bourlet, *Traité des Bicycles et Bicyclettes Suivi d'une Application à la Construction des Vélodromes* (Gauthier-Villars et fils, Paris, 1894).

[2] C. Bourlet, *Nouveau Traité des Bicycles et Bicyclettes. Equilibre et Eirection* (Gauthier-Villars et fils: Masson et Cie, Paris, 1898).

[3] C. Bourlet, *Nouveau Traité des Bicycles et Bicyclettes. Le Travail* (Gauthier-Villars et fils: Masson et Cie, Paris, 1898).

[4] N. P. Craig and K. I. Norton, Characteristics of track cycling, Sports Med. **31**, 457 (2001).

[5] R. Lukes, J. Hart, and S. Haake, An analytical model for track cycling, J. Sports Eng. Technol. **226**, 143 (2012).

[6] B. Fitton and D. Symons, A mathematical model for simulating cycling: applied to track cycling, Sports Eng. **21**, 409 (2018).

[7] G. de Groot, E. Welbergen, L. Clusen, J. Clarus, J. Cabri, and J. Antonis, Power, muscular work, and external forces in cycling, Ergonomics **37**, 31 (1994).

[8] G. J. van Ingen Schenau, Cycle power: a predictive model, Endeavour **12**, 44 (1988).

[9] J. C. Martin, D. L. Milliken, J. E. Cobb, K. L. McFadden, and A. R. Coggan, Validation of a mathematical model for road cycling power, J. Appl. Biomech. **14**, 276 (1998).

[10] C. Clanet, I. Sachet, S. Dorel, C. Cohen, B. Morel, M. Bowen, P. Samozino, and E. Brunet, Temporal power of a cycling sprinter: experiments and effective time theory, Proc. R. Soc. B **292**, 20242649 (2025).

[11] P. Barratt, SRM torque analysis of standing starts in track cycling, in *The Engineering of Sport* (Springer, Paris, 2009), Vol. 7, pp. 443–448.

[12] This regulation has applied since the 1992 Summer Olympics in Barcelona.

[13] https://www.phyling.fr/.

[14] B. Blocken, T. van Druenen, Y. Toparlar, F. Malizia, P. Mannion, T. Andrianne, T. Marchal, G. J. Maas, and J. Diepens, Aerodynamic drag in cycling pelotons: New insights by CFD simulation and wind tunnel testing, J. Wind Eng. Ind. Aerodyn. **179**, 319 (2018).

[15] H. Abel, Optimisation de l'aérodynamique cycliste/vélo en cyclisme sur piste, Ph.D. thesis, École doctorale de l'Institut polytechnique de Paris, 2025.

[16] D. E. Hall and J. C. Moreland, Fundamentals of rolling resistance, Rubber Chem. Technol. **74**, 525 (2001).

[17] J. K. Moore, M. Hubbard, A. L. Schwab, and J. D. G. Kooijman, Accurate measurement of bicycle parameters, in *Proceedings, Bicycle and Motorcycle Dynamics 2010: Symposium on the Dynamics and Control of Single Track Vehicles, 20–22 October 2010, Delft, The Netherlands* (Delft University of Technology, Delft, The Netherlands, 2010).